Journal of Power Sources 195 (2010) 341–353

Contents lists available at ScienceDirect

Journal of Power Sources

journal homepage: www.elsevier.com/locate/jpowsour

New hybrid inorganic–organic polymer electrolytes based on $Zr(O(CH_2)_3CH_3)_4$, glycerol and EMIm-TFSI ionic liquid

Malathi Jeyapandian[a], Sandra Lavina[a], Savitha Thayumanasundaram[a], Hiroyuki Ohno[c], Enrico Negro[a], Vito Di Noto[a,b,*,1]

[a] Dipartimento di Scienze Chimiche, Università di Padova, Via Marzolo 1, I-35131 Padova (PD), Italy
[b] Istituto di Scienze e Tecnologie Molecolari, ISTM-CNR and INSTM, Dipartimento di Scienze Chimiche, Via Marzolo 1, I-35131 Padova (PD), Italy
[c] Department of Biotechnology, Tokyo University of Agriculture and Technology, Koganei, Tokyo 184-8588, Japan

ARTICLE INFO

Article history:
Received 1 December 2008
Received in revised form 26 May 2009
Accepted 26 June 2009
Available online 7 July 2009

Keywords:
Hybrid inorganic–organic material
Ionic liquid
Vibrational spectroscopy
Thermal analysis
Broad band dielectric spectroscopy

ABSTRACT

This report presents detailed studies on the elemental analysis, vibrational spectroscopy, thermal stability and electrical spectroscopy of two new hybrid inorganic–organic polymers which have been synthesised by a sol–gel method using glycerol and zirconium(IV)butoxide as precursors. These materials have been doped by means of 1-ethyl-3-methylimidazolium bis(trifluoromethylsulfonyl)imide (EMIm-TFSI) ionic liquid (IL), which is insoluble in water. The elemental composition of the obtained polymers $[Zr(C_6O_5H_{11})]$ (**1**) and $[Zr(C_{11}O_4H_{31})]$ (**2**) has been determined by CHN analysis and by ICP-AES measurements. FT-IR and FT-Raman spectroscopy investigations have been performed to study the molecular structure of the polymers and the interactions of EMIm-TFSI with the host networks. Differential scanning calorimetry measurements show the presence of at least one glass transition temperature (T_g) in both **1** and **2** materials. The broadband dielectric spectroscopic measurements have been carried out between 10^{-2} Hz to 10 MHz from −100 °C to 100 °C with a 5 °C step. The conductivities of the polymers **1** and **2** have been found to be in the order of 10^{-8} to 10^{-11} S cm^{-1} at 25 °C, so they can be defined as dielectric materials. After doping **2** with EMIm-TFSI, the conductivity at 25 °C of the obtained complex $[Zr(C_{11}O_4H_{31})]_{15}$/(EMIm-TFSI) (**2′**) increased three orders of magnitude resulting ca. 10^{-5} S cm^{-1}. The permittivity spectra revealed two relaxation bands which were attributed to the α relaxation modes of the polymer networks.

1. Introduction

Solid polymer electrolytes are of growing importance in solid state electrochemistry. The most important application of polymer electrolytes is for high energy density batteries and high power density capacitors [1–4]. To improve the performance of energy storage devices much effort is currently directed towards the preparation of new hybrid inorganic–organic systems [2,3]. Several three-dimensional networks based on organic macromolecules bridged by inorganic atoms like Ti, Zr and Si have been synthesised [5–9]. The conductivity of the systems depends upon the doping salt and on the size of the coordination nests in the materials. The preparation of hybrid organic–inorganic polymers has attracted much attention because such hybrids may show controllable physical and chemical properties, such as optical, electrical and mechanical behaviours, by combining the properties of both organic polymers and inorganic compounds.

Ionic liquids (ILs) are organic salts with a very low melting point (<100 °C) which are the focus of many investigations as they show excellent chemical stability, non-flammability, non-volatility, non-toxicity, negligible vapour pressure, high ionic conductivity and wide electrochemical potential window [10]. The development of non-volatile and non-flammable ion conductive materials is important to improve both the safety and the durability of electrochemical devices. Due to these properties, ionic liquids are being used in various electrochemical devices. Recent research works by various groups point towards the excellent performance of ILs in electrochemical devices such as solar cells [11], lithium batteries [12], fuel cells [13] and supercapacitors [14].

All solid polymer electrolytes have advantages including mechanical stability, thermal stability, simple processing, and safety. However, their conductivity and electrochemical potential window is still insufficient for practical applications. The addition of ionic liquid to the polymer electrolytes distinctively improves their electrochemical stability and ionic conductivity. Ionic liquids have been incorporated in polymer matrices to develop ionic liquid-incorporated gel polymer electrolytes (ILGPEs). In order to improve the mechanical properties of ILGPEs the "composite approach" has been already attempted. The first polymer electrolytes based on ionic liquids are composites prepared from a preformed polymer

* Corresponding author at: Dipartimento di Scienze Chimiche, Università di Padova, Via Marzolo 1, I-35131 Padova (PD), Italy.
E-mail address: vito.dinoto@unipd.it (V. Di Noto).
[1] Active ACS, ECS and ISE member.

0378-7753/$ – see front matter © 2009 Published by Elsevier B.V.
doi:10.1016/j.jpowsour.2009.06.088

and a liquid organic salt [15,16]. In this method, inorganic nanoparticle fillers have been introduced into the ILGPEs to enhance the mechanical strength of the system and to increase the ionic conductivity of the material by lowering its crystallinity. Several ionic liquids have been tested to select the most suitable electrolytes for ultracapacitors, covering imidazolium, phosphonium, ammonium and pyrrolidinium groups. The better performance in terms of energy and power density is obtained for ILs based on imidazolium cations owing to their relatively high ionic conductivity and lower viscosity. In particular, the highest performance in supercapacitors is exhibited by the 1-ethyl-3-methylimidazolium bis(trifluoromethylsulfonyl)imide (EMIm-TFSI) thanks to its low viscosity and despite its low conductivity with respect to other imidazolium-type ILs [4].

In the present study, ionic liquids have been incorporated in hybrid polymer matrices to develop new hybrid inorganic–organic polymer electrolytes (H-IOPEs). The hybrid host polymers are considered as the development of the "composite approach" in which the EMIm-TFSI incorporation is applied. Thus, a new class of hybrid inorganic–organic polymer based on Zr(IV)butoxide and glycerol has been synthesised using a sol–gel method [17] and incorporating ionic liquids into the polymer matrix. It should be highlighted that ILs are very peculiar systems owing to their characteristic dual behaviour. Indeed, from one side ILs act as ionic materials endowed with integer charges; from the other side they behave like low-weight molecular organic solvents endowed with a dipolar moment. This twofold activity makes the inclusion of ILs in bulk H-IOPEs a crucial procedure in order to modulate in these systems: (a) the mechanical and thermal performance; as a matter of fact, ILs act as good plasticizers; and (b) the electric properties in terms of ionic conductivity and double-layer capacity. Actually, it is expected that ILs play a crucial role in increasing the interfacial polarization phenomenon of IL-doped H-IOPEs. Consequently, the latter become suitable systems for application in supercapacitor devices. Insights on the structure of the polymers have been determined by vibrational spectroscopy (FT-IR and FT-Raman) and DFT calculations. The polymer has been subjected to thermal analysis using differential scanning calorimetry (DSC). The electrical response of the polymer has been studied by broadband dielectric spectroscopy at the frequency range from 10^{-2} Hz to 10 MHz and temperature range −100 °C to +100 °C. The cyclic voltammetry measurements have been carried out in order to determine the electrochemical window of the prepared materials.

2. Experimental

2.1. Reagents

Zr(IV)butoxide 80 wt% solution in 1-buthanol (Sigma–Aldrich) has been used as received. Glycerol (Aldrich, ACS grade) has been dried at 100 °C for 3 days under low pressure (10^{-2} mbar) and kept in Ar atmosphere (dry box with <1 ppm H_2O and <1 ppm O_2). Solvents have been purified by standard methods and sealed under argon atmosphere on 4 Å molecular sieves to prevent contamination by moisture. 1-Ethyl-3-methylimidazolium bis(trifluoromethylsulfonyl)imide (EMIm-TFSI) (Kanyo Chemical Co., INC) has been used as received.

2.2. Synthesis

The materials were prepared according to a two-step protocol as shown in Scheme 1. In the first step the hybrid network materials were synthesised by adding 3.2 mL of glycerol to 20 mL of Zr(IV)butoxide solution drop by drop in an inert atmosphere of Ar (until the molar ratio of the two reagents was 1:1). The reaction vessel was kept under stirring at ambient temperature

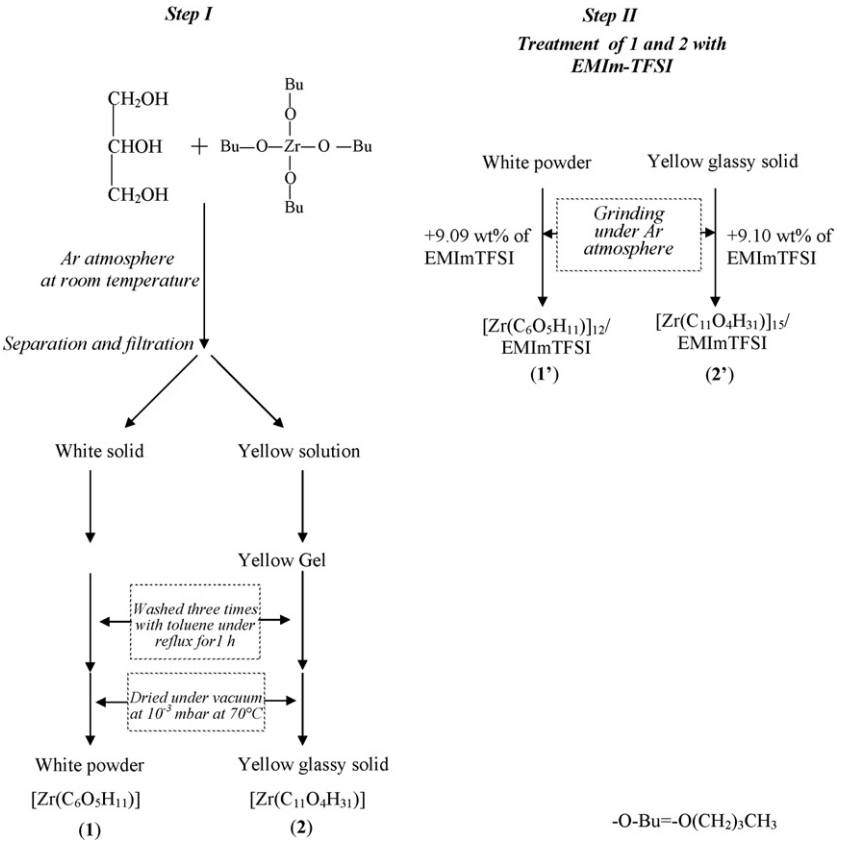

Scheme 1. Syntheses of hybrid polymers **1** and **2** (step I) and of the doped materials **1′** and **2′** (step II).

overnight. A yellow solution and a white solid have been recovered. The white solid portion has been separated and washed three times with toluene at reflux for 1 h yielding a white powder. A gel has been obtained from the yellow solution. It has been washed three times with toluene at reflux for 1 h. Both the white powder and the yellow gel have been dried under vacuum (10^{-3} mbar) at 70 °C. A yellow glassy solid has been obtained from the dried gel. In the second step, the doped $[Zr(C_6O_5H_{11})]_{12}$/EMIm-TFSI and $[Zr(C_{11}O_4H_{31})]_{15}$/EMIm-TFSI materials were obtained by adding 9.09 wt% and 9.10 wt% of 1-ethyl-3-methylimidazolium bis(trifluoromethylsulfonyl)imide (EMIm-TFSI) ionic liquid to previously prepared materials $[Zr(C_6O_5H_{11})]$ (**1**) (white material) and $[Zr(C_{11}O_4H_{31})]$ (**2**) (yellow material), respectively. The mixtures were manually grinded in a mortar under Ar atmosphere. The obtained doped materials $[Zr(C_6O_5H_{11})]_{12}$/EMIm-TFSI and $[Zr(C_{11}O_4H_{31})]_{15}$/EMIm-TFSI were singled out as **1′** and **2′**, respectively.

2.3. Instruments and methods

The percentage of C, H and N in samples has been determined by CHN analyzer. The amount of zirconium in the products has been determined by ICP-AES measurements using the emission line λ(Zr) = 339.198 nm. Solutions suitable for ICP-AES analysis have been prepared by treating the polymers with a dilute solution of HCl. The ICP-AES measurements have been carried out using a Spectroflame Modula sequential and simultaneous spectrometer equipped with a capillary cross-flow nebulizer (Spectro Analytical, Kleve, Germany). Zr determination has been performed using a plasma power of 1.2 kW, a radio-frequency generator of 27.12 MHz and an argon gas flow in nebulizer, auxiliary, and coolant of 1 L min^{-1}, 0.5 L min^{-1} and 14 L min^{-1}, respectively.

FT-IR spectra in the medium infrared (MIR) region have been measured by using a Nicolet FT-IR Nexus spectrometer equipped with a triglycine sulfate (TGS) detector at a resolution of 4 cm^{-1}.

FT-Raman spectra have been obtained with a Nicolet FT-Raman Module attached to a Nexus FT-IR system. The spectra were collected at an angle of 90° with a spectral slit width of 4 cm^{-1}. Each spectrum was the result of the accumulation and averaging of 2000 scans. The spectra were recorded at room temperature with the samples sealed under argon in Pyrex glass NMR tubes.

DSC measurements have been performed using a DSC 2920 differential scanning calorimeter operating under an N_2 flux of 70 cm^3 min^{-1}, equipped with the LNCA low temperature attachment. The analysis has been performed from −100 °C to +100 °C, with a heating rate of 10 °C min^{-1}. A sample of about 15 mg was sealed in an aluminum pan. DSC measurement has been carried out for three cycles.

Electrochemical measurements have been performed using a Bio Logic multi channel VSP potentiostat/galvanostat in the potential range of −1.5 to 10 V at a sweeping rate of 20 mV s^{-1}. The electrochemical stability window was determined by cyclic voltammetry measurements (CV), sandwiching a film of the material with a thickness ranging from 45 μm to 200 μm between two symmetric circular platinum blocking electrodes with a diameter of 1.5 cm. The CV measurements were carried out adopting a two-electrode geometry with one of the two Pt electrodes working simultaneously as quasi-reference and counter electrode. The explicit cathodic (E_{CL}) and anodic (E_{AL}) limits were 0 V and 4 V, respectively. E_{CL} and E_{AL} correspond to the voltages where the CV curve exhibited a current increase higher than 10% with respect to the lowest current value detected in the explored region.

Measurements of electrical spectra have been carried out in the frequency range 10^{-2} Hz to 10 MHz using an Alpha analyser. The measurements have been carried out in the temperature range −100 °C to +100 °C after cooling the measuring cell from room temperature down to −100 °C at 5 °C min^{-1}. The measuring cell temperature has been controlled by means of a Novocontrol Quatro cryostat operating with a N_2 gas jet heating and cooling system. The samples in the form of a pellet were sealed under argon atmosphere in a home-made Teflon conductivity cell between two gold-plated stainless steel parallel electrodes. Before each analysis the cell constant was determined by micrometrical measurements of the electrolyte electrode contact surface and of the distance between electrodes. The electrodes have a diameter of 20 mm and the thickness of samples ranged from 45 μm to 120 μm. The complex permittivity, $\varepsilon^* = \varepsilon' - i\varepsilon''$, has been converted into the complex conductivity, $\sigma^* = \sigma' + i\sigma''$, by using the equation $\sigma^* = i\omega\varepsilon^*$ ($\sigma' = \omega\varepsilon''$, $\sigma'' = \omega\varepsilon'$), where $\omega = 2\pi f$ (f = frequency in Hz). The temperature has been measured with an accuracy better than ±0.1 °C.

2.4. Computational methods

The hybrid systems shown in Scheme 2a and b have been submitted to the geometry optimization task performed by applying the Universal forcefield [18–21] using the Forcite program of the Materials Studio package [22]. The geometry optimization is refined by using the DMol3 program [23,24] included in the Materials Studio package [22] for the local density approximation described by Perdew and Wang [25] (PWC functional), and double numerical basis set except that no 'p' functions are used on hydrogen (dnd) as implemented in DMol3.

First-principle energy calculations were conducted using density functional theory implemented in an all-electron DFT code, DMol3 [23,24]. A double numerical basis set with double polarization (dnd) [23] was used. The exchange-correlation interaction was treated by generalized gradient approximation with PWC functional [26]. A convergence criterion of 10^{-6} a.u. on the total energy was used in the self-consistent field (SCF) calculations.

Finally, the fundamental vibrational frequencies for the optimized structures were calculated using the PWC (dnd) method as implemented in DMol3.

The internal modes were identified by visualizing the associated atomic motion with the aid of the animation of each computed mode built in the DMol3 package.

3. Results and discussion

3.1. Composition of *1* and *2*

The elemental composition of materials **1** and **2** is given in Table 1 along with the molar ratios with respect to zirconium content. The proposed stoichiometry for the repeating units is $[Zr(C_6O_5H_{11})]$ and $[Zr(C_{11}O_4H_{31})]$ for **1** (white) and **2** (yellow) materials, respectively. It can be observed that the composition of the two compounds is markedly different. The syntheses shown in Scheme 1 took place owing to substitution of the butoxide group of Zr(IV)butoxide precursor through a nucleophilic attack by the glycerol followed by buthanol elimination. The substitution reaction of the butoxide groups coordinated to Zr atoms decreases the stoichiometry ratio n_C/n_{Zr} of the products. The ratio $n_C/n_{Zr} = 6$ suggests the presence of two glycerol units for each Zr atom in the **1** network, thus indicating that the complete substitution of butoxide ligand happened to produce **1** material (Scheme 2a). The ratio $n_C/n_{Zr} = 11$ is lower than $n_C/n_{Zr} = 16$ of Zr(IV)butoxide reagent, but it is higher than the $n_C/n_{Zr} = 6$ of **1**. This information allows us to hypothesize that in **2** the substitution reaction of butoxide ligands did not proceed completely and two butoxide groups and one molecular fragment coming from glycerol can be found for each Zr atom in the **2** material (Scheme 2b).

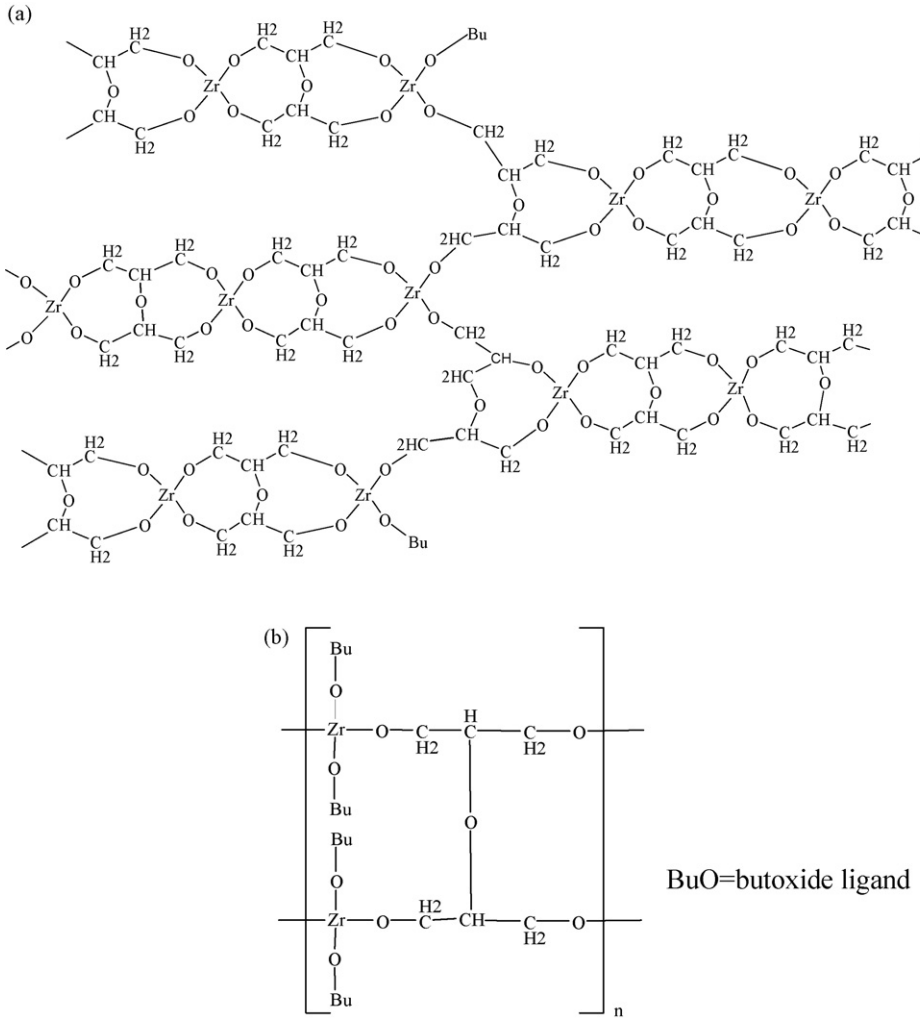

Scheme 2. Structural hypotheses for **1**, [Zr($C_6O_5H_{11}$)] (a), and **2**, [Zr($C_{11}O_4H_{31}$)] (b), materials.

3.2. FT-IR and FT-Raman analysis

Figs. 1 and 2 show the FT-IR and FT-Raman spectra of **1**, **1′**, **2**, **2′** and EMIm-TFSI. Table 2 reports the observed absorption and scattering bands together with their relative intensities for the materials **1**, **1′** and EMIm-TFSI. The 7th column in Table 2 gives selected vibrational frequencies calculated by DFT method on the basis of the structural hypothesis for the material **1** shown in Scheme 3a. DFT computations were performed as explained in more detail in Section 3.3. The 8th column in Table 2 shows the correlative assignments for the observed bands and the description of the vibrational modes of the calculated vibrational frequencies. Table 3 has the same structure of Table 2 but it is referred to the materials **2**, **2′** and EMIm-TFSI.

The first feature observed in the IR spectra of the prepared polymers **1** and **2** is the absence of the stretching and bending vibrations of OH groups (see Fig. 1). This suggests that a complete condensation of alcohol groups coming from pristine glycerol took place for both **1** and **2** systems.

In the frequency region between 2800 cm^{-1} and 3000 cm^{-1} the expected absorption and scattering bands related to the stretching of the CH bonds have been observed in the IR and Raman spectra, respectively. Among these latter bands the unexpected stretching and bending peaks typical of methyl group are revealed in **1**, which indicate that butyl groups are present in **1**. To take care of this observation we hypothesized that butoxides are present in **1** as the terminal groups. Indeed, the intensity of the vibrational bands due to the CH_3 groups is lower in the spectra of **1** with respect to the intensity values measured in the spectra of **2**. Apart from their different profiles, no significant frequency shift has been observed between the vibrational bands of **1** and **2** in this region.

Table 1
Composition of [Zr($C_6O_5H_{11}$)] (**1**) and [Zr($C_{11}O_4H_{31}$)] (**2**) materials. Molar ratios referred to Zr atoms are shown.

Compound	C[a] (wt%)	H[a] (wt%)	Zr[b] (wt%)	O[c] (wt%)	n_C/n_{Zr}	n_H/n_{Zr}	n_O/n_{Zr}
[Zr($C_6O_5H_{11}$)] (**1**)	29.61	4.32	34.61	31.46	6.50	11.30	5.20
[Zr($C_{11}O_4H_{31}$)] (**2**)	41.99	9.58	28.53	19.90	11.18	30.40	3.98

[a] Analyzed by CHN analyser.
[b] Determined by ICP-AES measurements.
[c] Determined as difference from 100%.

Table 2
FT-IR and FT-Raman band assignments for the [Zr($C_6O_5H_{11}$)] (**1**), {[Zr($C_6O_5H_{11}$)]$_{12}$/EMIm-TFSI} (**1′**) and EMIm-TFSI.

Observed frequencies (cm^{-1})[a]						Calculated frequencies[b]	Band assignments[c]	Ref.
1		**1′**		EMIm-TFSI				
IR	Raman	IR	Raman	IR	Raman			
					3307 (vw)		ν^s(HCCH)$_{ring}$, $\nu^s{}_{ip}$(ring)	[27]
			3168 (vw)	3160 (w)	3176 (vw)		ν^s(HCCH)$_{ring}$, $\nu^s{}_{ip}$(ring)	[28]
				3122 (w)	3130 (vw)		ν(NC(H)NCH)$_{ring}$	[28]
				3109 (sh,w)	3107 (vw)		ν^a(CH_3(N)HCH)	[28]
	3052 (m)		3053 (m)					
				2991 (vw)	2993 (sh,vw)		ν^a(CH_3(N)HCH)	[28]
				2970 (vw)	2970 (m)		ν^a(CH_2HCH), ν^a(HCH)$_{ethyl}$	[28]
2956 (vs)		2953 (w)					ν^a(CH_3)	[31]
				2950 (vw)	2953 (m)		ν^a(CH_3HCH)$_{terminal}$	[28]
2929 (vs)	2932 (vs)	2924 (w)	2931 (s)				ν^a(CH_2)	[31]
					2931 (w)		ν^s(CH_3HCH)$_{ring}$	[28]
	2906 (s)		2906 (s)				ν^s(CH_3)	[31]
					2891 (w)		ν^s(CH_3HCH)$_{terminal}$, ν^s(CH_3)	[28]
2868 (vs)	2871 (vs)	2870 (vs)	2872 (vs)				ν^s(CH_3)	[28]
		2858 (w)					ν^s(CH_2)	[28]
		2831 (sh,vw)						
					2841 (vw)		ν^s(CH_3HCH)$_{terminal}$	[28]
	2733 (w)		2733 (w)					
2704 (w)	2710 (w)						ν(CH)	[31]
			2571 (vw)					
	1604 (w)		1604 (m)					
	1585 (w)		1585 (w)					
		1572 (vw)		1574 (w)	1570 (vw)		$\nu^{s,a}{}_{ip}$(ring), ν(CH_3(N)), ν(CH_2(N)), ν^s(CN)	[28]
1523 (w)								
				1471 (w)	1473 (sh,vw)		$\nu^a{}_{ip}$(ring), ν(CH_3(N))	[28]
1464 (m)	1465 (s)	1458 (w)	1464 (s)				δ(CH_3), sr(CH_2)	[31]
				1456 (vw)	1454 (w)		δ^s(CCH HCC), δ^s(CH_3(N)HCH), δ^a(CH_3HCH)$_{terminal}$	[28,31]
1433(w)								
		1431 (w)		1431 (vw)	1431 (sh,vw)		$\nu^a{}_{ip}$(ring), ν(CH_3(N)CN), δ^s(CH_3(N)HCH)	[28]
		1419 (w)			1421 (m)		$\nu^a{}_{ip}$(ring), ν(CC), ν((N)CH_2), ν(CH_3(N)CN)	[28]
				1392 (sh)	1387 (w)		$\nu^a{}_{ip}$(ring), ν(CC), δ(CH_2(N)), ν(CH_3(N)CN), ν(CH_2(N))	[28]
1377 (m)	1378 (w)	1375 (sh,w)	1379(w)				δ^s(CH_3)	[31]
		1352 (m)		1352 (s)			ν^a(SO_2)	[28]
		1333 (m)	1333 (w)	1333 (s)	1336 (m)		ν^a(SO_2), $\nu^s{}_{ip}$(ring), ν(CC), ν(CH_2(N)), ν(CH_3(N)CN)	[28]
1297 (vw)	1296 (m)		1296 (m)				τ_{ip}(CH_2)	[31]
1261 (w)		1273 (w)				1260	τ + r(CH_2)	[31]
	1250 (w)		1250 (w)			1252	τ + r(CH_2)	[31]
			1244 (m)		1242 (s)		ν^a(SO_2), δ^s(CF_3)	[28]
1228 (w)	1225 (w)	1227 (w)	1225 (m)	1226 (m)		1229	τ + r(CH_2)	[31]
	1211 (w)		1211(w)			1212	τ + r(CH_2)	[31]
		1194 (s)		1190 (vs)			ν^a(CF_3)	[32]
				1138 (m)	1136 (m)		ν^s(SO_2)	[32]
1120 (sh,s)	1115 (w)	1120 (sh,s)	1117 (w)			1118	δ(ZrOBu) + δ(Bu) + δ(gly) + δ(OZrO)	
1103 (vs)		1101 (vs)					ν^s(COCOC)	[28]
					1090 (w)		ν(CC), $\nu^s{}_{ip}$(ring)	[34]
1074 (sh,m)	1064 (w)	1074 (sh,s)	1064 (w)				ν_{oop}(CCO)	[33]
		1059 (vs)		1057 (s)			$\nu^a{}_{ip}$(ring), ν(CC), ν^a(SNS), τ(NCH_3)	[32]
1040 (sh,m)	1030 (w)	1040 (sh,m)	1030 (m)			1041	ν(CCO) T gly	
					1024 (w)		CF, $\nu^s{}_{ip}$(ring), ν(CH_3(N)), ν(CH_2(N))	[27]
1005 (sh,w)	1003 (vw)	1005 (sh,m)	1003 (m)			1005	δ(gly) + δ(Bu) + ν(CCO) T gly + δ(ZrO)	
970 (m)	965 (vw)	966 (m)	966 (m)			975	ν(CO) T gly, δ(gly T), ν(CCO) T gly + δ(CH_2)	[33]
				958(vw)	960 (vw)		ν (CC)	[28]
927 (m)	927 (vw)	931 (m)	928 (w)			926	ν(CO) G gly, δ(Bu) + δ(ZrOgly) + ν(glyT&G) + δ(ZrO) + ν(CCO) Tgly	[33]
901 (w)	901 (vw)	901 (w)	901 (w)			901	δ(ZrOglyOZr) + δ(glyOgly) + δ(ZrO) + ν(gly)	
856 (m)	866 (w)	856 (m)	866 (m)			864	ν^{sec}(C–C–C)	[33]
				843 (vw)			δ_{ring}(NC(H)N), δ(CCH)	[28]
823 (vw)	827 (w)		827 (m)			823	ν^{pri}(C–C–C), δ(gly T) + δ(Bu) + δ(glyOgly), ν^a(ring)	[33]
810 (vw)	810 (vw)		812 (w)			809	ν(ZrO) tetrahedral, δ(ZrOBu) + δ(ZrOgly) + δ(ZrO) + ν(ring)	[35]
		789 (w)		791 (w)	793 (vw)		$\delta^a{}_{ring}$(HCCH), ν(CS)	[28]
	785 (m)		785 (s)			787	ν(ZrO) tetrahedral, δ(ZrO) + ν(gly)	
		762 (vw)		762 (w)			$\delta^a{}_{ring}$(HCCH), ν^s(SNS)	[28]
			740 (m)	741 (w)	740 (vs)		δ(CH_3(N)), δ(CH_2(N)), δ^s(CF_3), $\delta_{ring,ip}$	[28]
727 (s)	721 (w)	721 (m)	712 (vw)			707	ν(ZrO), collective breath of the network, breath of the double ring	[35]
				702 (vw)	702 (vw)		$\delta^a{}_{ring,ip}$, ν(CH_2(N)), ν(CH_3(N)CN)	[28]
671 (m)	669 (w)	660 (m)				671	δ(C–C–O), δ(ZrOC) + δ(glyOgly), δ(ZrO) + δ(ring)	[33]
	650 (w)					646	Wagging of the double ring	
			650 (w)	650 (w)	650 (vw)		$\delta^a{}_{ring,oop}$, δ(SNS)	[28]
	623 (w)		623 (w)			622	Wagging of the double ring	
		617 (w)		615 (m)			$\delta^a{}_{ring,oop}$, δ^a(SO_2), ν(CH_3(N)CN)	[28]
		602 (w)	598 (m)	602 (m)	598 (m)		$\delta^s{}_{ring,ip}$, δ^a(SO_2), ν(CH_3(N)CN)	[28]

Table 2 (*Continued*)

Observed frequencies (cm^{-1})[a]						Calculated frequencies[b]	Band assignments[c]	Ref.
1		**1′**		EMIm-TFSI				
IR	Raman	IR	Raman	IR	Raman			
599 (m)						601	Collective breath of the network, δ(ZrO) + δ(ring)	
		571 (w)		571 (m)	571 (w)		$\delta^{s}_{ring,ip}$, $\delta^{a}(CF_3)$	[32]
					551 (w)		δ^{s} (SO_2)	[32]
	521 (m)		521 (m)			516	ν(ZrO) + δ(double ring)	
		513 (w)		515 (m)			$\delta^{a}(CF_3)$	[32]
457 (s)						457	δ(C–C–O), collective bending and wagging of the network	

[a] Relative intensities of observed bands are reported in parentheses: vs, very strong; s, strong; m, medium; w, weak; vw, very weak; sh, shoulder.

[b] Calculated by DFT methods as described in the experimental section on the basis of the structural model shown in Scheme 2a.

[c] ν, stretching; δ, bending, τ, twisting; r, rocking; sr, scissoring; a, antisymmetric mode; s, symmetric mode; ip, in-plane; oop, out-of-plane; T, trans; G, gauche; gly, glycerol fragment. The description of the calculated vibrational modes is reported in italic.

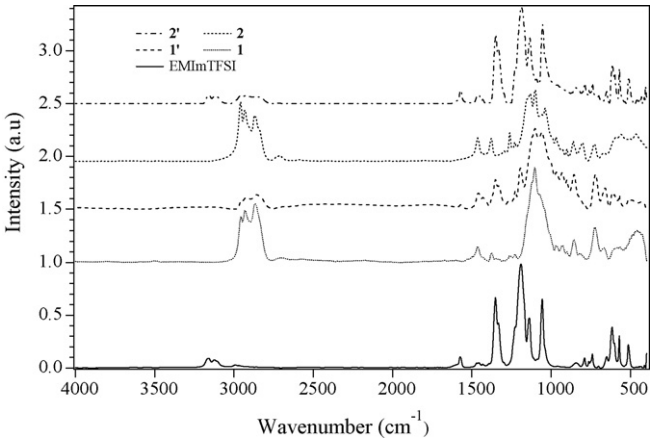

Fig. 1. FT-IR spectra of **1**, **1′**, **2**, **2′** and EMIm-TFSI.

The stretching and bending bands of CO and CCO groups are expected in the frequency region from 850 cm^{-1} to 1200 cm^{-1}. In this region it is possible to note that: (a) the bands localized at 1174 cm^{-1}, 1134 cm^{-1} and 951 cm^{-1} were detected for the material **2** only. These vibrations were obtained also from the DFT calculations performed on the structural model for the material **2** (Schemes 2b and 3b), where they resulted to be mainly composed by some bending of butoxide groups coordinating the Zr atoms (see Table 3); (b) the difference in wavenumber was observed in the out-of-plane stretching vibration of the CCO group in **1** and **2** materials (1074 (IR) – 1064 cm^{-1} (R) for the **1** and 1059 (IR) – 1055 cm^{-1} (R) for the **2**). This difference suggested that the **1** network is stiffer than the **2** and this is due to the higher concentration of butoxide groups in **2** with respect to material **1**; (c) the characteristic vibrational bands for glycerol moiety in trans conformation was found at 970 cm^{-1} for **1** and **2**, while the band witnessing the presence of a glycerol fragment in gauche conformation was revealed at 927 cm^{-1} and 931 cm^{-1} for **1** and **2**, respectively. In the case of pristine glycerol it is localized at 924 cm^{-1}, which means that the force constant of the vibrational modes of glycerol moiety became stronger in bridging Zr atoms in the **1** and **2** networks with respect to that of the pristine molecule. The above facts are in accordance with the structural hypotheses for the materials **1** and **2** (Scheme 3).

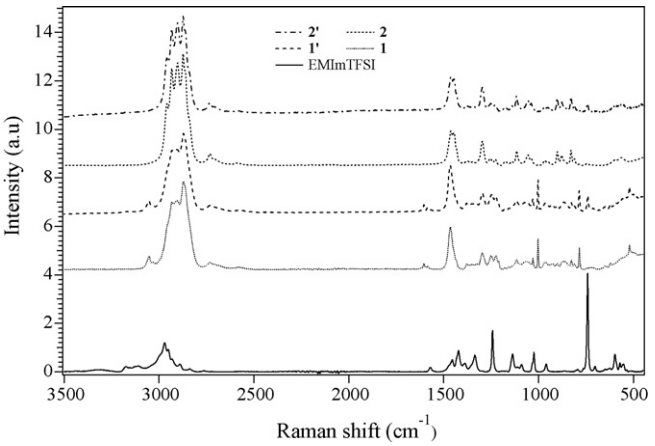

Fig. 2. Raman spectra of **1**, **1′**, **2**, **2′** and EMIm-TFSI.

It should be highlighted that, this difference in wavenumbers was satisfactorily reproduced by DFT calculations (Tables 2 and 3). The presence of tetrahedral ZrO_4 units in all the prepared materials is proved by the 810 cm^{-1} band [35]. The vibration localized at 785 cm^{-1} was observed in material **1**, while the vibration localized at 746 cm^{-1} is detected exclusively in material **2**.

In summary, as expected in the IR spectra of **1** and **2** materials most of the bands are peaking at the same frequencies and exhibit different shapes and relative intensities. The observed differences were satisfactorily reproduced by the hypothesised structural models (Scheme 2).

The main difference in the Raman spectra of **1** and **2** is the presence of the sharp and intense bands at 1003 cm^{-1}, 785 cm^{-1}, and 521 cm^{-1} for **1** (Fig. 2). These bands are related to the vibrational modes of the ZrO_4 units. This observation suggests that ZrO_4 units are more symmetric and homogeneously distributed in bulk material **1** than those detected in **2**.

In conclusion, the vibrational spectroscopy studies of the materials **1** and **2** confirmed that they are network polymers in which Zr atoms are tetrahedrally coordinated by glycerol organic bridges with material **1** structurally more homogeneous than **2**. In material **2** a higher concentration of butoxide ligand is present with respect to **1**.

The spectrum of EMIm-TFSI was exhaustively assigned elsewhere [27,28]. The vibrational modes of this IL were detected in the IR and Raman spectra of **1′** and **2′** materials with no substantial shift in frequency with respect to the pristine IL. In particular, it is worth to highlight that no significant frequency shift was detected: (a) for the IR bands peaking at 741 cm^{-1}, 762 cm^{-1}, and 791 cm^{-1}, which are vibrational modes diagnostic of ion pair formation [29]; and (b) for the Raman band localized at 740 cm^{-1}, which is assigned to the symmetric bending of the CF_3 group. This latter band is usually used to study the chemical interactions with the surroundings. Results show that no significant interactions took place between the ionic liquid and the hosting network materials in **1′** and **2′** systems. Indeed, in agreement with other investigations [30], the structure of the bulk-like nature of ionic liquid is maintained in the host polymers.

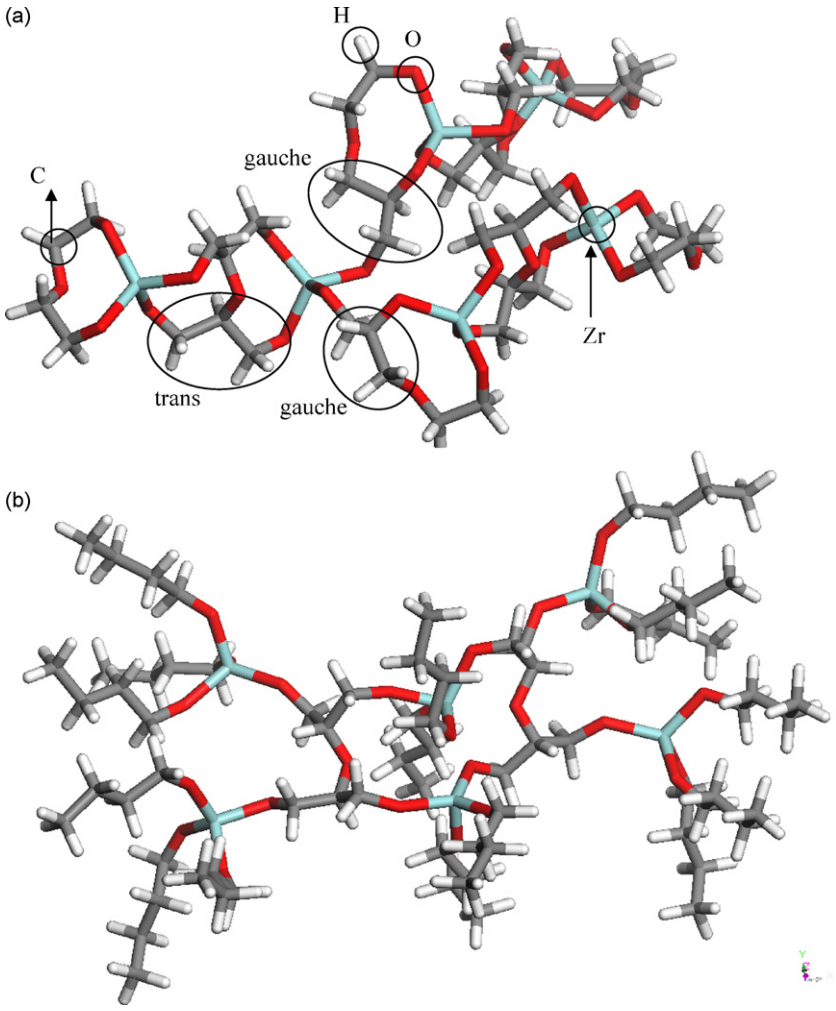

Scheme 3. Structural models proposed for **1** (a) and **2** (b) materials.

In the IR and Raman spectra of **1**′ and **2**′ most of the observed frequencies can be correlated to the pristine polymer or to the IL without any significant change in their frequency positions. One exception can be observed for the Raman band localized in the spectrum of **1**′ at 712 cm^{-1} which was attributed to the collective breathing vibration of the host polymer network. This peak in the Raman spectrum of pristine **1** is localized at 721 cm^{-1}. Another exception is observed in the IR spectrum of **1**′, where the band revealed at 660 cm^{-1} is correlated to the band of pristine polymer at 671 cm^{-1}. These differences in band positions suggest that the inter-chain interactions of the network **1** are weakened after doping the material with the IL, which thus acts as a plasticizer.

3.3. *Determination of **1** and **2** structural hypotheses*

The structural hypotheses for the prepared materials **1** and **2** have been devised on the basis of their analytical composition and vibrational studies. The structures hypothesized for the repeating units of the prepared materials **1** and **2** are reported in Scheme 2a and b respectively. The basic structure of **1** consists of two Zr atoms bridged together by two glycerol molecules which are condensed with each other through one oxygen atom bridge. The asymmetric repeating units are then composed of rings with 8 vertexes. The basic structural repeating unit of **2** consists of four Zr atoms bridged together by two glycerol molecules which are condensed by one oxygen bridge. The coordination of each Zr atom is completed by two butoxide groups (Scheme 2b).

The soundness of the proposed structural hypotheses has been proved by performing DFT calculations on the hypothesised repeating unit which is representative of the networked polymers shown in Scheme 3a and b respectively for **1** and **2** materials. In Scheme 3a it is possible to observe that the **1** representative structural unit is endowed predominantly with trans glycerol units. From the IR spectrum of **1** material both trans and gauche conformations were detected. Thus, it is to be hypothesized that material **1** is more complicated with respect to the simple ribbon structure with 8 vertex rings proposed in the basic unit shown in Scheme 2a. Therefore, to account of the experimental evidences it was necessary to impose that the hypothesised polymer network consists of ribbon fragments linked together through gauche glycerol units. Thus, **1** is composed by 6 Zr atoms linked together by 8-vertex rings endowed with one networking center (Scheme 2a). In order to carry out DFT calculations it was necessary to assume the oligomer shown in Scheme 3.

The fragment **2**, which was obtained by following the same procedure of **1**, is composed by 6 Zr atoms linked together by glycerol bridges as previously described and terminated by butoxide groups (Scheme 2b). The frequencies calculated for the **1** and **2** oligomers which are representative of networked polymers **1** and **2** are reported in the 7th column of Tables 2 and 3, respectively. It is

Table 3
FT-IR and FT-Raman band assignments of the [Zr($C_{11}O_4H_{31}$)] (**2**), {[Zr($C_{11}O_4H_{31}$)]$_{15}$/EMIm-TFSI} (**2′**) and EMIm-TFSI.

Observed frequencies (cm^{-1})[a]						Calculated frequencies[b]	Band assignments[c]	Ref.
2		**2′**		EMIm-TFSI				
IR	Raman	IR	Raman	IR	Raman			
					3307 (s)		$\nu^s(HCCH)_{ring}$, $\nu^s{}_{ip}$(ring)	[27]
		3157 (w)		3160 (w)	3176 (s)		$\nu^s(HCCH)_{ring}$, $\nu^s{}_{ip}$(ring)	[28]
		3120 (w)		3122 (w)	3130 (vw)		$\nu(NC(H)NCH)_{ring}$	[28]
				3109 (sh,w)	3107 (s)		$\nu^a(CH_3(N)HCH)$	[28]
				2991 (vw)	2993 (sh,vw)		$\nu^a(CH_3(N)HCH)$	[28]
				2970 (vw)	2970 (m)		$\nu^a(CH_2HCH)$, $\nu^a(HCH)_{ethyl}$	[28]
2958 (vs)	2959 (s)	2951 (w)	2958 (s)				$\nu^a(CH_3)$	[31]
				2950 (vw)	2953 (m)		$\nu^a(CH_3HCH)_{terminal}$	[28]
2931 (vs)	2933 (vs)	2926 (w)	2933 (vs)				$\nu^a(CH_2)$	[31]
					2931 (vw)		$\nu^s(CH_3HCH)_{ring}$	[28]
		2902 (s)	2902 (vs)				$\nu^s(CH_3)$	[31]
					2891 (vw)		$\nu^s(CH_3HCH)_{terminal}$, $\nu^s(CH_3)$	[28]
2872 (vs)	2873 (vs)		2873 (vs)				$\nu^s(CH_3)$	[31]
2864 (sh,w)	2862 (sh,vs)	2860 (w)	2862 (sh,vs)				$\nu^s(CH_2)$	[31]
					2841 (vw)		$\nu^s(CH_3HCH)_{terminal}$	[28]
					2764 (vw)			
2727 (w)	2732 (w)	2729 (vw)	2733 (m)					
2710 (w)	2709 (vw)	2710 (vw)	2706 (w)				ν(CH)	[31]
2588 (w)	2588 (w)							
		1572 (w)		1574 (w)	1570 (vw)		$\nu^{s,a}{}_{ip}$(ring), $\nu(CH_3(N))$, $\nu(CH_2(N))$, ν^s(CN)	[28]
				1471 (w)	1473 (sh,vw)		$\nu^a{}_{ip}$(ring), $\nu(CH_3(N))$	[28]
1464 (m)	1463 (m)	1462 (w)	1464 (s)				$\delta(CH_3) + sr(CH_2)$	[31]
		1454 (w)	1448 (s)	1456 (vw)	1454 (w)		δ^s(CCH HCC), $\delta^s(CH_3(N)HCH)$, $\delta^a(CH_3HCH)_{terminal}$	[28,31]
1431 (w)	1446 (m)							
		1431 (vw)		1431 (vw)	1431 (sh,vw)		$\nu^a{}_{ip}$(ring), $\nu(CH_3(N)CN)$, $\delta^s(CH_3(N)HCH)$	[28]
					1421 (w)		$\nu^a{}_{ip}$(ring), ν(CC), $\nu((N)CH_2)$, $\nu(CH_3(N)CN)$	
				1392 (sh)	1387 (w)		$\nu^a{}_{ip}$(ring), ν(CC), $\delta(CH_2(N))$, $\nu(CH_3(N)CN)$, $\nu(CH_2(N))$	[28]
1377 (m)	1378 (vw)		1379 (w)				$\delta^s(CH_3)$	[31]
		1350 (s)		1352 (s)			$\nu^a(SO_2)$	[28]
		1331 (s)		1333 (s)	1336 (w)		$\nu^a(SO_2)$, $\nu^s{}_{ip}$(ring), ν(CC), $\nu(CH_2(N))$, $\nu(CH_3(N)CN)$	[28]
1295 (w)	1296 (m)	1298 (sh,w)	1296 (m)				$\tau_{ip}(CH_2)$	[31]
1261 (m)							$\tau + r(CH_2)$	[31]
	1253 (w)		1252 (w)				$\tau + r(CH_2)$	[31]
					1242 (s)		$\nu^a(SO_2)$, $\delta^s(CF_3)$	[28]
1228 (w)	1228 (w)	1227 (w)	1228 (w)				$\tau + r(CH_2)$	[31]
		1188 (vs)		1190 (vs)			$\nu^a(CF_3)$	[32]
	1174 (w)		1174 (w)			1174	δ(ZrOBu) + δ(HCOCH) + $\delta(CH_2CHCH_2)$	
				1138 (m)	1136 (w)		$\nu^s(SO_2)$	[32]
1134 (vs)	1139 (w)	1134 (s)	1140 (w)			1134	δ(Bu) + δ(ZrOBu)	
	1115 (m)		1117 (m)			1118	δ(ZrOBu) + δ(Bu) + δ(gly) + δ(OZrO)	
1101 (vs)		1094 (w)				1107	ν^s(COCOC), δ(ZrOgly-ring)	[31]
					1090 (vw)		ν(CC), $\nu^s{}_{ip}$(ring)	[34]
1059 (s)	1055 (w)	1055 (vs)	1055 (w)			1055	ν_{oop}(CCO), δ(glyOgly) + δ(ZrOBu)	[33]
				1057 (s)			$\nu^a{}_{ip}$(ring), ν(CC), ν^a(SNS), $\tau(NCH_3)$	[32]
1038 (vs)	1039 (w)	1038 (sh,m)	1039 (w)			1041	ν(CCO) T gly	
					1024 (w)		CF, $\nu^s{}_{ip}$(ring), $\nu(CH_3(N))$, $\nu(CH_2(N))$	[27]
	1003 (vw)					1002	δ(gly) + δ(Bu)	
973 (m)	968 (vw)		969 (w)			975	ν(CO) T gly, δ(glyT)	[33]
		958 (w)		958 (vw)	960 (vw)		ν(CC)	[28]
	951 (w)		951 (w)			950	δ(T gly) + δ(Bu)	
		931 (w)				936	ν(CO) G gly, δ(Bu) + δ(ZrOgly) + ν(glyT&G)	[33]
901 (w)	901 (w)	899 (w)	901 (m)			900	δ(ZrOglyOZr) + δ(glyOgly)	
862 (m)	879 (w)	870 (w)	877 (m)			872	δ(ZrOBu) + δ(ZrOgly) + δ(glyG), ν^{sec}(C–C–C)	[33]
		845 (w)		843 (vw)			δ_{ring}(NC(H)N), δ(CCH)	[28]
	829 (w)	835 (w)	829 (m)			828	ν^{pri}(C–C–C), δ(T gly) + δ(Bu) + δ(glyOgly)	[33]
802 (m)	811 (w)		812 (w)			809	ν (ZrO) tetrahedral, δ(ZrOBu) + δ(ZrOgly)	[35]
		789 (m)		791 (w)	793 (vw)		$\delta^a{}_{ring}$(HCCH), ν(CS)	[28]
		762 (w)		762 (w)			$\delta^a{}_{ring}$(HCCH), ν^s(SNS)	[28]
	746 (w)					743	δ(Bu) + δ(ZrOgly)	
		741 (m)	742 (m)	741 (w)	740 (vs)		$\delta(CH_3(N))$, $\delta(CH_2(N))$, $\delta^s(CF_3)$, $\delta_{ring,ip}$	[28]
		739 (m)				738	δ(Bu) + δ(gly)	
727 (m)						729	ν(ZrO), collective breath in mode of the network	[35]
		700 (w)		702 (vw)	702 (vw)		$\delta^a{}_{ring,ip}$, $\nu(CH_2(N))$, $\nu(CH_3(N)CN)$	[28]
671 (w)						670	δ(CCO), δ(ZrOC) + δ(glyOgly)	[33]
		650 (w)		650 (w)	650 (vw)		Ring op δ^a, δ^a (SNS)	[28]
		613 (m)		615 (m)			$\delta^a{}_{ring,oop}$, $\delta^a(SO_2)$, $\nu(CH_3(N)CN)$	[28]
		600 (m)		602 (m)	598 (w)		$\delta^s{}_{ring,ip}$, $\delta^a(SO_2)$, $\nu(CH_3(N)CN)$	[28]
596 (m)			596 (w)			596	Collective breath in mode of the network	
		569 (m)		571 (m)	571 (vw)		$\delta^s{}_{ring,ip}$, $\delta^a(CF_3)$	[32]
561 (m)	563 (vw)			561 (w)				

Table 3 (*Continued*)

Observed frequencies (cm^{-1})[a]						Calculated frequencies[b]	Band assignments[c]	Ref.
2		**2′**		EMIm-TFSI				
IR	Raman	IR	Raman	IR	Raman			
					551 (vw)		δ^s (SO_2)	[32]
		511 (m)		515 (m)			δ^a (CF_3)	[32]
465 (m)	449 (w)		461 (w)			463	δ (C–C–O), collective bending of the network	[31]

[a] Relative intensities of observed bands are reported in parentheses: vs, very strong; s, strong; m, medium; w, weak; vw, very weak; sh, shoulder.
[b] Calculated by DFT methods as described in the experimental section on the basis of the structural model shown in Scheme 2a.
[c] ν, stretching; δ, bending, τ, twisting; r, rocking; sr, scissoring; a, antisymmetric mode; s, symmetric mode; ip, in-plane; oop, out-of-plane; T, trans; G, gauche; gly, glycerol fragment. The description of the calculated vibrational modes is reported in italic.

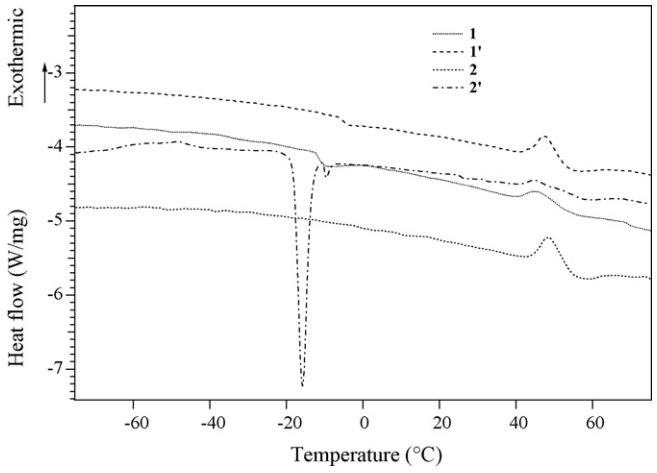

Fig. 3. DSC curves of **1**, **1′**, **2** and **2′** materials collected at a heating rate of 10 °C min^{-1} from −100 °C to 100 °C (3rd scan).

to be pointed out that the calculated vibrational modes are in good agreement with the experimental frequencies.

3.4. Thermal and electrochemical stability

Fig. 3 shows the DSC profiles of **1**, **2**, **1′** and **2′** materials collected from −100 °C to +100 °C. The glass transition temperatures of **1**, **2**, **1′** and **2′** are given in Table 4. DSC curves show two glass transition temperatures for **1** at −11 °C (T_{g1}) and 49 °C (T_{g2}). The T_{g1} and T_{g2} of **1′** were detected at −5 °C and 50 °C, respectively. T_{g2} of **2** and **2′** was revealed at 51 and 50 °C, respectively. T_{g2} values of **2**, **2′**, **1** and **1′** are very close with each other, thus suggesting that the thermal features of these materials are very similar. In **2′** a further endothermic peak associated to the melting of the ionic liquid (EMIm-TFSI) has been observed at −16 °C. This peak witnesses that, with respect to the **1′** material, in the bulk **2′** material ionic liquid domains with a larger size are present [36].

The DSC results are in accordance with vibrational studies and confirmed that the addition of EMIm-TFSI to **1** and **2** materials does not affect significantly the structure and the interactions existing between the polymer chains.

Table 4
Glass transition temperatures (T_g) and melting point (T_{mp}) of **1**, **2**, **1′**, **2′** and EMIm-TFSI materials as detected from DSC measurements from −100 °C to +100 °C.

Sample	T_{mp}	T_{g1}	T_{g2}
1		−11 °C	49 °C
1′		−5 °C	50 °C
2			51 °C
2′	−16 °C		50 °C
EMIm-TFSI[a]	−16 °C		

[a] Taken from [37].

Taken together, DSC results are in accordance with vibrational spectroscopic and DFT studies thus confirming that **1′** network is more compact than **2′**. On this basis, it is possible to hypothesize that, with respect to **1′** material, the amount of free volume in **2′** is higher. Thus, it is expected that ionic liquid clusters embedded in bulk **2′** network are characterized by larger sizes which are easily detectable by DSC analyses.

The electrochemical stability of **1**, **2**, **1′** and **2′** systems has been tested by cyclic voltammetry. All the investigated materials exhibited an electrochemical window up to 4 V, thus indicating that **1′** and **2′** networks are promising materials to explore and to improve for the development of hybrid polymers for the application in ultracapacitors.

3.5. Broadband dielectric spectroscopy

Broadband dielectric spectroscopy investigations have been performed in order to study the electrical properties of **1**, **2**, **1′** and **2′** materials. The spectra of the real component of conductivity (σ') of **1**, **1′**, **2** and **2′** (data not shown) exhibited a strong dependence on frequency, thus indicating that dispersive phenomena are taking place in these compounds. In these spectra some plateaus were observed whose frequency ranges depend on the temperature and on material compositions. The $\sigma'(\omega)$ values at the plateaus correspond to the σ_{dc} values. The σ_{dc} values vs. the inverse of temperature are reported in Fig. 4. The three vertical lines reported in Fig. 4 show the DSC transitions previously described (Table 4). It should be observed that a transition at about −66 °C is detected in conductivity measurements which was not revealed in DSC profiles. The transition revealed by DSC measurements at −11 °C is confirmed in σ_{dc} profiles. The second glass transition observed in DSC curves of the **1**,

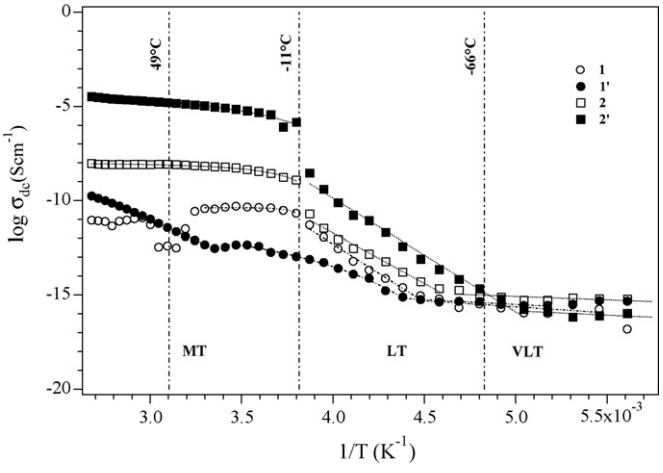

Fig. 4. Dependence of σ_{dc} on the reciprocal of temperature for **1**, **1′**, **2** and **2′**.

Table 5
Activation energies obtained fitting with Arrhenius-type and VTF equations of dc conductivity and relaxation peak positions of **1**, **1′**, **2** and **2′**.

Region		*i*	Sample							
			1	Fitting	**1′**	Fitting	**2**	Fitting	**2′**	Fitting
VLT	E_i (kJ mol^{-1})	σ_{dc}	12 ± 5	A	10 ± 1	A	7 ± 2	A	8.5 ± 4	A
		α-1	14.6 ± 1.2	A	5 ± 6	A				
		α-2	11 ± 6	H			81 ± 1	A	87 ± 7	A
		β					21 ± 2	A	53 ± 9	A
	T_0 (K)	α-2	106 ± 23							
LT	E_i (kJ mol^{-1})	σ_{dc}	101 ± 6	A	3.1 ± 0.9	V	102 ± 5	A	115 ± 4	A
		α-1	21.9 ± 0.7	A	3.1 ± 0.3	H	25 ± 2	A	46.1 ± 0.8	A
		α-2	0.29 ± 0.01	H			6.5 ± 1.8	H	2.4 ± 0.4	H
	T_0 (K)	σ_{dc}			192 ± 7					
		α-1			170 ± 0					
		α-2	221.1 ± 0.5				149 ± 12		177 ± 5	
MT	E_i (kJ mol^{-1})	σ_{dc}	2.4 ± 2.3	V	0.14 ± 0.06, 38 ± 8	V, V	0.36 ± 0.04	V	1.5 ± 0.4	V
		α-1			32 ± 1	H	0.22 ± 0.01	H	0.40 ± 0.07	H
		α-2					0.25 ± 0.02	H		
	T_0 (K)	σ_{dc}	260 ± 3		260 ± 0, 105 ± 22		246 ± 2		224 ± 9	
		α-1			105 ± 0		243.8 ± 1.6		225 ± 9	
		α-2					227 ± 2			

A = Arrhenius-type fit; V = Vogel–Tamman–Fulcher-type fit; H = Vogel–Tamman–Fulcher–Hesse-type fit. VLT = very low temperature (from −100 °C to −66 °C); LT = low temperature (from −66 °C to −11 °C); MT = medium temperature (higher than −11 °C).

1′, **2** and **2′** materials is shown with a line located at 49 °C in Fig. 4.

It can be summarised that the dependence of the σ_{dc} values on the inverse of temperature reflects the temperature regions delimited by the DSC transitions in Fig. 3 and Table 4. The conductivity regions were indicated as follows: "VLT" (Very Low Temperatures) from −100 °C to −66 °C; "LT" (Low Temperatures) from −66 °C to −11 °C; and "MT" (Medium Temperatures) for temperatures higher than −11 °C. The σ_{dc} curves were fitted by Arrhenius (A) or by Vogel–Tamman–Fulcher-type equation (V). The pseudo-activation energies and the T_0 values thus determined are summarised in Table 5.

In VLT the σ_{dc} curves: (a) present values ranging between 10^{-15} S cm^{-1} and 10^{-16} S cm^{-1} for all the materials; (b) were satisfactorily fitted by Arrhenius-type equations and the obtained activation energies are 12 kJ mol^{-1}, 10 kJ mol^{-1}, 7 kJ mol^{-1} and 8 kJ mol^{-1} for **1**, **1′**, **2** and **2′** materials, respectively. In LT the dependence on temperature of σ_{dc} of the **1**, **2**, and **2′** materials was still of Arrhenius type. The activation energy was of about 101 kJ mol^{-1} and 115 kJ mol^{-1} for the pristine polymers and **2′** material respectively. It should be observed that in LT the activation energy is one order of magnitude higher with respect to that measured at VLT, thus indicating that between VLT and LT regions a further order–disorder transition event takes place at about −66 °C. Indeed, when the hybrid polymer changes from a more ordered to a more disordered solid state its electrical conductivity on temperature rises with a different slope.

In MT regions, the σ_{dc} dependence on $1/T$ of **1**, **2** and **2′** materials exhibits VTF behaviour. It should be observed that the temperature between LT and MT regions is coincident with T_{g1} of **1**. The activation energies of **1**, **2** and **2′** in MT are of the order of 2.4 kJ mol^{-1}, 0.36 kJ mol^{-1} and 1.5 kJ mol^{-1}, respectively (see Table 4). In **1** the VTF behaviour extends up to 30 °C, where a steep decrease of the electrical performance is observed which was attributed to the structural reorganization of the polymer network corresponding to T_{g2} event. In MT the σ_{dc} values for **2′** are about three orders of magnitude higher with respect to that of **2** owing to the effect of the ionic liquid embedded in bulk material. The σ_{dc} vs. $1/T$ curves of **1′** is somewhat different from the other samples: (a) the Arrhenius behaviour was observed from −80 °C to −45 °C, (b) three VTF-type behaviours were distinguished in the regions from −45 °C to 0 °C, from 0 °C to 25 °C and from 25 °C to 100 °C which are endowed with the activation energies 3.1 kJ mol^{-1}, 0.14 kJ mol^{-1} and 38 kJ mol^{-1}, respectively. The influence of IL in network **1** is very different from that of **2** material.

Taken together, these results suggest that: (a) the effect of IL in material **2** does not alter the conduction mechanism, but increases strongly the conductivity; (b) the electrical performance of the **1** is strongly modulated by the presence in bulk network of IL. Results show that conductivity profiles are correlated to the structure of materials. Therefore, it is suggested that EMIm-TFSI was hosted in bulk **2** material owing to direct interactions with hybrid ribbons. In this way, long-range charge migrations are promoted which are responsible of the conductivity increase in **2′** system. In material **1′** it is hypothesised that ionic liquid domains are confined inside nano-pores of supporting polymer. Thus EMIm-TFSI, owing to nano-porosities present in bulk **1** network, do not contribute to the long range charge migration for $T < T_{g2}$.

Fig. 5a–d presents the spectra vs. frequency and temperature of the imaginary component of permittivity (ε'') of the materials **1**, **1′**, **2** and **2′**, respectively. At low frequencies the three-dimensional plots (Fig. 5) show an increase of ε'' which was attributed to the electrode polarization event. As expected, the intensity of the electrode polarization phenomenon increases as the sample temperature rises.

For **1** material (Fig. 5a) two relaxation bands are revealed which were indicated as α-1 and α-2. The lower frequency peak (α-1) is overlapped with the electrode polarization phenomenon. It should be observed that the decrease of conductivity of **1** at high temperatures corresponds to a decrease of the intensity of the electrode polarization event (Fig. 5a).

Fig. 5b shows that at $T > 35$ °C the electrode polarization phenomenon of **1′** material is more intense than that of **1**. These results are easily explained considering that the electrode polarization phenomenon is correlated to the σ_{dc} of the materials.

The analysis of spectra of Fig. 5c and d shows that in **2** and **2′** three further relaxation bands can be distinguished, indicated as α-1, α-2 and β.

To gain more information on the conductivity mechanism and on the molecular and macromolecular relaxations of the materials the complex dielectric spectra were exhaustively simulated by the equation [33]:

$$\varepsilon^* = \frac{\sigma_{dc}}{i\omega\varepsilon_0}\frac{(i\omega\tau_{el})^{\gamma}}{1+(i\omega\tau_{el})^{\gamma}} + \sum_k \frac{\Delta\varepsilon_k}{\{1+(i\omega\tau_k)^{\beta_k}\}^{\alpha_k}} + \varepsilon_\infty \quad (1)$$

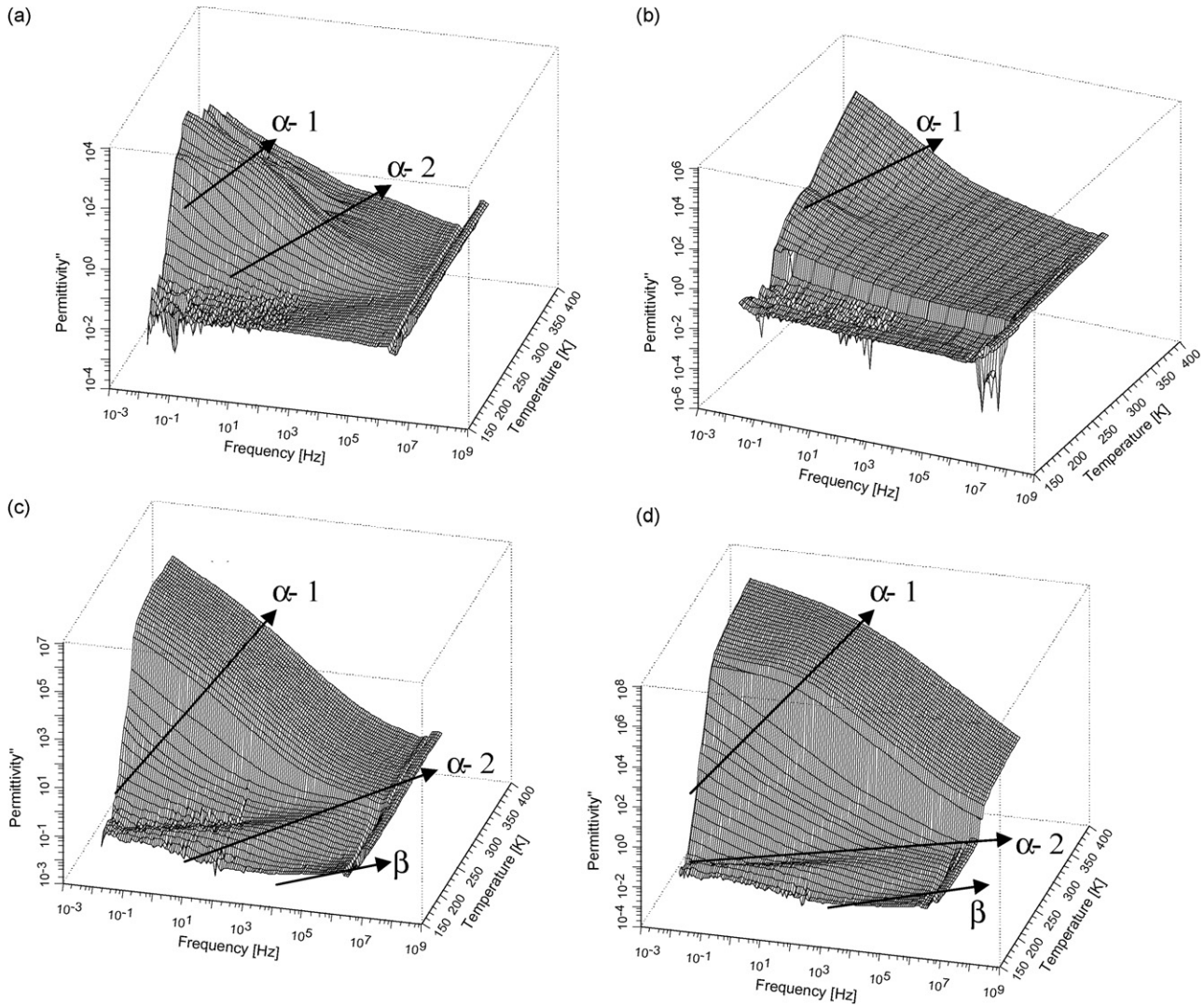

Fig. 5. Dependence of the imaginary component of permittivity on frequency and temperature for **1** (a), **1′** (b), **2** (c) and **2′** (d).

where σ_{dc} is the dc conductivity, α_k and β_k are the shape parameters describing the asymmetric and symmetric broadening of the k-th relaxation peak, $\tau_k = 1/2\pi f_k$ is the dielectric relaxation time of the k-th peak (f_k is the frequency of peak maximum), $\Delta\varepsilon_k$ is the relaxation strength, and τ_{el} is the relaxation time associated to the electrode polarization phenomenon.

The fitting of the experimental spectra was performed by using: (a) two relaxation bands for **1**; (b) one peak for **1′** material; and (c) three relaxation modes for **2** and **2′** networks. The dependence of the relaxation times vs. the inverse of temperature thus determined is shown in Fig. 6. It can be noticed that the relaxation mode α-1, peaking at low frequencies, is detected in all the investigated materials. α-2, which is observed in samples **1**, **2** and **2′**, is peaking nearly at the same position in both **2** and **2′** materials, while it is observed at higher frequencies in the case of **1**. β mode was revealed in **2** and **2′** materials. The three temperature ranges previously detected in the σ_{dc} profiles were also revealed in the dependence of relaxation times on the inverse of temperature.

In the VLT region, α-1 of **1** and **1′** shows Arrhenius-type dependences on $1/T$ with values of activation energies close to that of σ_{dc} (see Table 5). In the VLT region, α-2 of **1** exhibits a VTFH-type behaviour with an activation energy similar to that of σ_{dc}. In VLT region, α-2 of **2** and **2′** show Arrhenius-type dependencies on temperature with activation energies of 81–87 kJ mol^{-1}, respectively. These activation energies are about one order of magnitude higher with respect to the corresponding σ_{dc} values of **2** and **2′** which resulted 7 and 8.5 kJ mol^{-1}, respectively (Table 5).

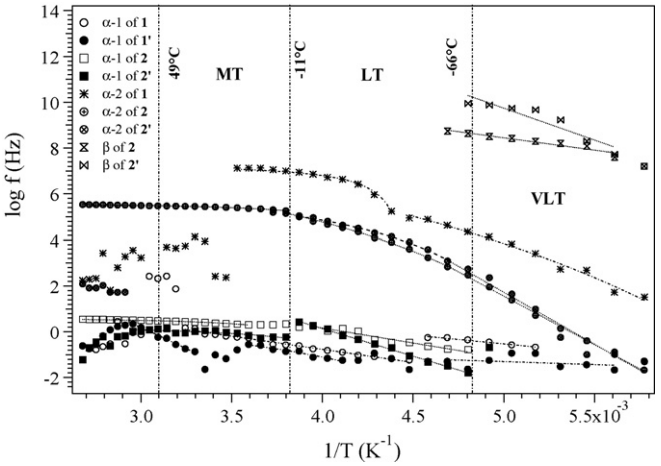

Fig. 6. Dependence of relaxation frequencies on the reciprocal of temperature for **1**, **1′**, **2** and **2′**.

The β relaxation of **2** and **2′** was detected in the high frequency wing of VLT region. β vs. $1/T$ shows an Arrhenius-type behaviour with the activation energies increasing from **2** to **2′**. On the basis of the proposed structural hypotheses we attributed the β mode of **2** to the relaxation event associated to the motion of butoxide side groups. Indeed, it is expected that the butoxide groups of **2** and **2′** materials are very mobile side groups.

The relaxation time α-1 of **1** presents Arrhenius dependence on temperature with a slope change at about −55 °C. This later phenomenon corresponds to an increase of activation energy from 15 kJ mol^{-1} to 22 kJ mol^{-1}. At 35 °C an abrupt variation of the relaxation time was registered which is in accordance with the σ_{dc} behaviour previously discussed.

The comparison of α-1 and σ_{dc} profiles of **1** indicates the three following analogies: (a) in the VLT regions the Arrhenius profiles are characterized by the same activation energies; (b) at $T > 35$ °C both σ_{dc} and α-1 show a transition associated to a structural reorganization of **1**; (c) in the LT and MT the average values of activation energy of both σ_{dc} and α-1 are of the same order of magnitude. These results suggest that in **1** α-1 is attributed to a relaxation mode correlated with the glass transition T_{g1}, which is responsible for the charge transfer mechanism in bulk **1**.

The α-2 observed in the dielectric spectra of material **1** showed two VTFH-type dependencies on temperature; the first from −80 °C to −55 °C and the second from −45 °C to 10 °C. This relaxation mode was attributed to a different α relaxation event directly correlated to segmental motion of host polymer thus witnessing that this mode is responsible of charge transfer mechanism in bulk material. Indeed, the activation energy of α-2 is close or lower than that of σ_{dc}. In **1′** α-1 shows two VTFH behaviours in both the LT and MT regions, with activation energies coinciding with those measured on σ_{dc} curves. These results suggest that in **1′** α-1 is associated to the backbone chain dynamics (T_{g1}) correlated to the charge transfer mechanism in bulk material. It should be observed that the IL embedded in bulk materials affects negligibly the main chain mobility of polymer **1**. Indeed, α-1 of **1′**: (a) is detected at frequencies slightly lower than those of **1**; (b) presents an activation energy very close to that of **1**.

In the LT region the α-1 mode of **2** and **2′** materials shows Arrhenius-type dependencies on temperature, with activation energies lower than those measured in the σ_{dc} profiles (Table 5). In the MT region, both the conductivity and α-1 relaxation times show analogues VTF and VTFH-type dependencies on temperature with activation energies values and ideal glass transition temperatures (T_0) which are quite coincident. The determined T_0 values are 50 °C lower than that of the T_{g2} glass transition. On this basis it can be hypothesised that the α-1 mode of **2** and **2′** is associated to the relaxation motions corresponding to the second glass transition temperature of the materials (T_{g2}). Thus, it is to be hypothesised that for temperatures higher than T_{g2} the dielectric relaxation event is strongly correlated to the charge transfer mechanism.

In the LT region, the α-2 of the **2** and **2′** materials show VTFH-type dependence on temperature. The activation energies of α-2 mode are nearly two orders of magnitude lower than those determined in σ_{dc} values while the T_0 values are coincident with the T_{g1} of the materials. In the MT, the α-2 of **2** presents on temperature a VTFH-type dependence which is substantially parallel to that of α-1 in the same region. In addition, in **2** the values of activation energy and T_0 of α-2 and α-1 are coincident. With respect to α-1 mode, α-2 was attributed to the segmental motion of backbone chains having faster relaxation motions.

Fig. 7 reports the dependence on the reciprocal of temperature of the dielectric strength ($\Delta\varepsilon$) of **1**, **1′**, **2** and **2′** relaxation modes. It can be noticed that the dielectric strength increases as the temperature rises. The $\Delta\varepsilon$ values of α-1 are higher than those of α-2 relaxations and similar in the **1** and **2** materials. In **2′**, the IL embedded in bulk material is responsible of the increase of the $\Delta\varepsilon$ values for both α relaxations. In **1′** $\Delta\varepsilon$ of the α-1 relaxation is close to that of **1** network.

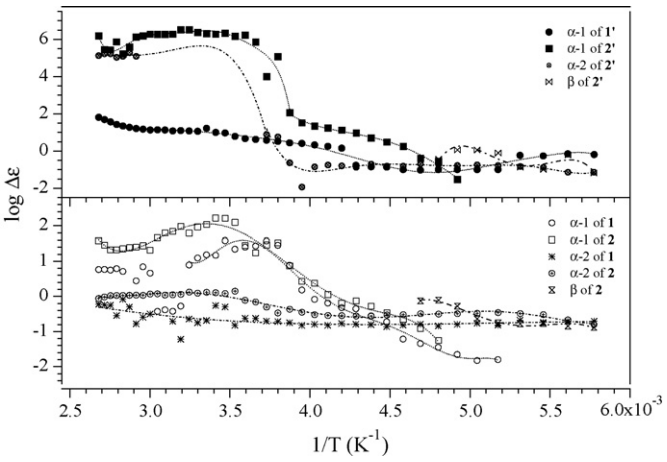

Fig. 7. Dependence of the dielectric strength on the reciprocal of temperature for **1**, **1′**, **2** and **2′**.

Taken together, all these results allow us to conclude that:

(a) two main-chain dynamics are revealed by BDS studies in both **1** and **2** hybrid networks, associated to α-1 and α-2 relaxation modes;
(b) the α-1 event in **1** and **2** is detected in the same frequency range and it is correlated to the charge transfer mechanism of materials;
(c) the effect of IL on the α-1 mode is more pronounced in **1** material;
(d) with respect to α-1, the α-2 event is revealed at higher frequencies and is not diagnostic of IL presence in bulk materials;
(e) β relaxation is found in materials **2** and **2′**. This relaxation mode was attributed to the butoxide side groups of the hybrid polymer network.

In summary the BDS studies above described are in accordance with the structural hypotheses proposed on the basis of vibrational spectroscopy investigations and DFT calculations and allowed us to reveal that the here reported hybrid materials are promising systems to improve in order to obtain materials suitable for the development of electrochemical devices such as supercapacitors.

4. Conclusions

This paper describes the preparation of two new inorganic–organic hybrid materials through sol–gel reactions with formulas [Zr($C_6O_5H_{11}$)] (**1**) and [Zr($C_{11}O_4H_{31}$)] (**2**). By doping **1** and **2** with the ionic liquid EMIm-TFSI, the hybrid materials **1′** and **2′** with composition [Zr($C_6O_5H_{11}$)]$_{12}$/EMIm-TFSI and [Zr($C_{11}O_4H_{31}$)]$_{15}$/EMIm-TFSI were obtained. Vibrational studies allowed us to: (a) obtain information on the structure of **1** and **2** materials; and (b) study the interactions between the IL and the host polymer matrix of **1′** and **2′** materials. Vibrational results indicated that **1** and **2** consist of hybrid inorganic–organic networks were Zr atoms are bridged together through glycerol molecules. The DSC and CV measurements showed that the prepared materials are thermally and electrochemically stable up to 100 °C and 4 V, respectively. The electrical properties of **1**, **2**, **1′** and **2′** have been analyzed by broadband dielectric spectroscopy in the frequency and temperature ranges 10^{-2} Hz to 10 MHz and −100 °C to +100 °C, respectively. After doping with EMIm-TFSI, the dc conductivity of **2** increased by three orders of magnitude. The values of

conductivity of **2**′ and **2** at 25 °C are of ca. 9.3×10^{-6} S cm^{-1} and 6.1×10^{-9} S cm^{-1}, respectively. In **1**′ network, the conductivity is slightly affected by the concentration of IL embedded in **1**. BDS results demonstrated that the electrical response of investigated hybrid materials are modulated by α and β relaxation phenomena. As expected the electrode polarization phenomenon resulted more pronounced in **2** than in **1** material. In addition, the hybrid system **2**′, obtained doping **2** with EMIm-TFSI, is a promising polymer electrolyte to improve in order to obtain materials with thermal and electrochemical stability and good conductivity for application in ultracapacitors.

Acknowledgements

Savitha Thayumanasundaram and Malathi Jeyapandian would like to thank MIUR (Italian Ministry for University and Research) for financial support through an Indo-Italian project from 2007 to 2008.

References

[1] M. Armand, W. Gorecki, S. Beranger, C. Michot, Proceedings of 8th International Symposium on Polymer Electrolytes, Santa Fe, NM, 2002, pp. 19–24.
[2] F.M. Gray, Polymer Electrolytes, RSC Materials Monographs, Royal Society of Chemistry, Cambridge, UK, 1997.
[3] B. Scrosati, R.J. Neat, Application of Electroactive Polymers, Chapman & Hall, London, 1993.
[4] W. Lu, K. Henry, C. Turchi, J. Pellegrino, J. Electrochem. Soc. 155 (2008) A361–A367.
[5] M. Popall, M. Andrei, J. Kappel, J. Kron, K. Olma, B. Olsowski, Electrochim. Acta 43 (1998) 1155–1161.
[6] S. Skaarup, K. West, B. Zachau-Christiansen, M. Popall, J. Kappel, J. Kron, G. Eichinger, G. Semrau, Electrochim. Acta 43 (1998) 1589–1592.
[7] V. Di Noto, M. Furlani, S. Lavina, Polym. Adv. Technol. 7 (1996) 759–767.
[8] V. Munchow, V. Di Noto, E. Tondello, Electrochim. Acta 45 (2000) 1211–1221.
[9] V. Di Noto, V. Zago, S. Biscazzo, M. Vittadello, Electrochim. Acta 48 (2003) 541–554.
[10] R.D. Rogers, K.R. Seddon, S. Volkov, Green Industrial Applications of Ionic Liquids Nano Science Series, Kluwer Academic Publishers, 2002.
[11] P. Wang, S.M. Zakeeruddin, P. Comte, I. Exnar, M. Gratzel, J. Am. Chem. Soc. 125 (2003) 1166–1167.
[12] B. Garcia, S. Lavallee, G. Perron, C. Michot, M. Armand, Electrochim. Acta 49 (2004) 4583–4588.
[13] M.A.B.H. Susan, A. Noda, S. Mitsushima, M. Watanabe, Chem. Commun. 8 (2003) 938–939.
[14] J.D. Stenger-Smith, C.K. Webber, N. Anderson, A.P. Chafin, K.K. Zong, J.R. Reynolds, J. Electrochem. Soc. 149 (2002) A973–A977.
[15] R.T. Carlin, J. Fuller, Chem. Commun. 15 (1997) 1345–1346.
[16] J. Fuller, A.C. Breda, R.T. Carlin, J. Electroanal. Chem. 459 (1998) 29–34.
[17] V. Di Noto, V. Zago, J. Electrochem. Soc. 151 (2004) A216–A223.
[18] A.K. Rappe, C.J. Casewit, K.S. Colwell, W.A. Goddard, W.M. Skiff, J. Am. Chem. Soc. 114 (1992) 10024–10035.
[19] C.J. Casewit, K.S. Colwell, A.K. Rappe, J. Am. Chem. Soc. 114 (1992) 10035–10046.
[20] C.J. Casewit, K.S. Colwell, A.K. Rappe, J. Am. Chem. Soc. 114 (1992) 10046–10053.
[21] A.K. Rappe, K.S. Colwell, C.J. Casewit, Inorg. Chem. 32 (1993) 3438–3450.
[22] http://www.accelrys.com/.
[23] B. Delley, J. Chem. Phys. 92 (1990) 508–517.
[24] B. Delley, J. Chem. Phys. 113 (2000) 7756–7764.
[25] J.P. Perdew, Y. Wang, Phys. Rev. B 45 (1992) 13244–13249.
[26] J.P. Perdew, J.A. Chevary, S.H. Vosko, K.A. Jackson, M.R. Pederson, D.J. Singh, C. Fiolhais, Phys. Rev. B 46 (1992) 6671–6687.
[27] N.E. Heimer, R.E. Del Sesto, Z.Z. Meng, J.S. Wilkes, W.R. Carper, J. Mol. Liq. 124 (2006) 84–95.
[28] J. Kiefer, J. Fries, A. Leipertz, Appl. Spectrosc. 61 (2007) 1306–1311.
[29] S. Abbrent, J. Lindgren, J. Tegenfeldt, A. Wendsjo, Electrochim. Acta 43 (1998) 1185–1191.
[30] A. Martinelli, A. Matic, P. Jacobsson, L. Borjesson, M.A. Navarra, S. Panero, B. Scrosati, J. Electrochem. Soc. 154 (2007) G183–G187.
[31] D. Lin-Vein, N.B. Colthup, W.G. Fateley, J.G. Grasselli, The Handbook of Infrared and Raman Charateristic Frequencies of Organic Molecules, Academic Press, Boston, MA, 1991.
[32] I. Rey, P. Johansson, J. Lindgren, J.C. Lassegues, J. Grondin, L. Servant, J. Phys. Chem. A 102 (1998) 3249–3258.
[33] V. Di Noto, M. Vittadello, S.G. Greenbaum, S. Suarez, K. Kano, T. Furukawa, J. Phys. Chem. B 108 (2004) 18832–18844.
[34] E.R. Talaty, S. Raja, V.J. Storhaug, A. Dolle, W.R. Carper, J. Phys. Chem. B 108 (2004) 13177–13184.
[35] K. Nakamoto, Infrared and Raman Spectra of Inorganic and Coordination Compounds, 4th ed., John Wiley and Sons, New York, 1986.
[36] J.H. Shin, W.A. Henderson, S. Passerini, J. Electrochem. Soc. 152 (2005) A978–A983.
[37] H. Ohno, Electrochemical Aspects of Ionic Liquids, John Wiley and Sons, New Jersey, 2005.